Overview of Predictive Simulation Capability Development for Crater Evolution and Ejecta in Continuum/Rarefied Flows

Andrew Weaver*
Geocent, Jacobs Space Exploration Group, NASA Marshall Space Flight Center, Huntsville, AL, 35808, USA

William Krolick† and Peter Liever‡
CFD Research Corporation, Jacobs Space Exploration Group, NASA Marshall Space Flight Center, Huntsville, AL, 35808, USA

Jeff West§
NASA Marshall Space Flight Center, Huntsville, AL, 35808, USA

As part of the Game Changing Development (GCD) Program funded by NASA's Space Technology Mission Directorate (STMD), the development of simulation capability for the prediction of extra-terrestrial plume surface interaction (PSI) environments has been undertaken by the Fluid Dynamics Branch at NASA/MSFC. The Predictive Simulation Capability (PSC) Element is focused on creating simulation capability for the reliable and accurate prediction of PSI in Martian (~650 Pa) and Lunar (vacuum) ambient environments. In this paper, an overview and brief status on one area of capability development through this GCD PSI project, capturing the effects of mixed continuum/rarefied flow on crater development and ejecta sheets, is presented with respect to capability enhancements, predictive tool maturation, and validation of the *Loci/GGFS* tool against PSI data in Martian and Lunar environments. Axisymmetric modeling, overset mesh/moving mesh, and multiple-species mixture modeling capabilities are verified against *Loci/CHEM*, and a demonstration of the capabilities is presented for the Apollo Lunar Module.

I. Nomenclature

alpha	=	solid volume fraction
D_e	=	nozzle exit diameter
M	=	Mach number
P_c	=	nozzle chamber pressure
P	=	static pressure
T	=	static temperature

---

* Senior Engineer, Fluid Dynamics Branch, and AIAA Senior Member.
† CFD Analyst, Fluid Dynamics Branch
‡ Senior Engineer, Fluid Dyamics Branch
§ AST Fluid Mechanics, Fluid Dynamics Branch

II. Introduction

Numerous human and robotic landers such as Apollo Lunar Module, the InSight robotic Mars Lander, and the Curiosity Mars Rover have landed on the Moon and Mars with a controlled descent from propulsive systems. In each of these landings, significant plume surface interaction (PSI) effects were observed, which includes surface cratering, view obscuration by plume-induced ejection of dust particles, and high-speed ejecta/debris transport. These PSI effects can pose significant risks to the Entry, Descent, and Landing (EDL) systems, nearby assets, and the mission and its crew by: (1) landing in the plume-induced crater, causing excessive tilting of the lander, (2) obscuring view of the surface below with eroded dust particles, and/or (3) high-speed ejecta/debris impacts to the vehicle or nearby assets driven by the plume flow. As NASA plans to land human landers on the Moon under the Artemis program, it is important to understand and mitigate these risks posed by PSI induced environments.

The approach taken by the Fluid Dynamics Branch at NASA Marshall Space Flight Center to understand and mitigate the risks posed by the PSI induced environments is to develop a simulation capability for the prediction of extra-terrestrial PSI environments. This work is part of the Game Changing Development (GCD) program, funded by NASA's Space Technology Mission Directorate (STMD) and aimed at creating a simulation capability for the reliable and accurate prediction of PSI in Martian (approximately 650 Pa) and Lunar (vacuum) ambient conditions. In addition to the predictive simulation capability, the GCD program also contains a companion Ground Testing Element for the development of focused datasets for validation of predictive capability as well as a Flight-focused Instrumentation Element. With both the simulation capability development and ground test data from the GCD program, the simulation tool can be validated against the relevant physics and applied to the intended applications.

The path to developing new capabilities for the reliable and accurate prediction of PSI environments is divided into four main tasks within the GCD project: (1) plume flow in low pressure environment modeling, (2) effect of mixed continuum/rarefied flow on crater development and ejecta sheets, (3) regolith particle phase modeling, and (4) gas-particle interaction modeling. Thus, there are separate plume flow and regolith modeling tasks as well as a task devoted to crater development and ejecta in low-pressure environments where regions of continuum and rarefied flows may exist. This latter task is the focus of this paper.

New modeling capabilities, including axisymmetric modeling, overset mesh with moving mesh, multi-species gas mixture modeling, preconditioning with boundary conditions, and turbulence models have been implemented into the multi-phase, multi-physics *Gas-Granular Flow Solver (GGFS)* simulation tool developed by CFD Research Corporation.[1] A brief overview and status on these newly developed capabilities will be discussed in Section III, with a particular focus on axisymmetric modeling, overset mesh/moving mesh, and multi-species gas mixture modeling. Beyond implementing new capabilities, the capabilities must be verified and evaluated before being production ready. Thus, gas flow solutions of relevant PSI environments are verified for each capability against a verified and validated CFD tool for plume flows, *Loci/CHEM*,[2-4] in Section III. A demonstration of current predictive simulation capabilities for crater evolution and ejecta will be presented in Section IV for the Apollo LM and Physics Focused Ground Test 1 (PFGT1) conducted through the GCD program. Section V of this paper includes several validation analyses in both Martian-like and Lunar-like environments, including *Loci/GGFS* simulations of cratering from a subsonic flow test[5] at the Planetary Aeolian Lab (PAL) conducted in a Martian-like environment and pre-test simulations of PFGT1.

III. Predictive Simulation Capability Development Status

In this section, an overview and brief status of predictive simulation capability development will be provided for several capabilities implemented into the gas-granular flow solver, *Loci/GGFS*.[1] These capabilities add computational efficiencies and higher-fidelity modeling to the existing tool capabilities. For example, both axisymmetric model and preconditioning in both the gas and solid phases can improve the computational efficiencies by taking advantage of symmetry (reduced computational mesh size) and accelerated convergence of the linear solver, respectively. Other capabilities, such as the overset mesh/moving mesh, multiple-species modeling, and turbulence modeling introduce additional physics to improve the fidelity of the simulations. For example, implementing an overset moving mesh capability into *Loci/GGFS* allows for the simulation of a landing vehicle during descent, including the transient PSI effects as the vehicle approaches the surface. Of each of these newly developed capabilities, three of them will be discussed in more detail in this section, with respect to solution verification against the computational fluid dynamics (CFD) solver, *Loci/CHEM*: axisymmetric modeling, overset mesh/moving mesh, and multiple-species modeling.

A. Axisymmetric Modeling Capability

Axisymmetric modeling can improve the computational efficiencies of CFD solvers like *Loci/GGFS* by taking advantage of axisymmetric fluid flows and reducing the computational domain from a full 3D geometry to a small pie slice. However, this capability must first be verified before being used in a production mode, and therefore three simulations have been performed to verify the solutions under conditions similar to the intended extraterrestrial landing environment: (1) gas-only, axisymmetric *Loci/GGFS* simulation of a representative Lunar lander plume, (2) gas-only, axisymmetric *Loci/CHEM* simulation of a representative Lunar lander plume, and (3) gas-granular, axisymmetric *Loci/GGFS* simulation of a representative Lunar lander plume with a regolith surface below the nozzle (see Fig. 1 below for a depiction of these three cases).

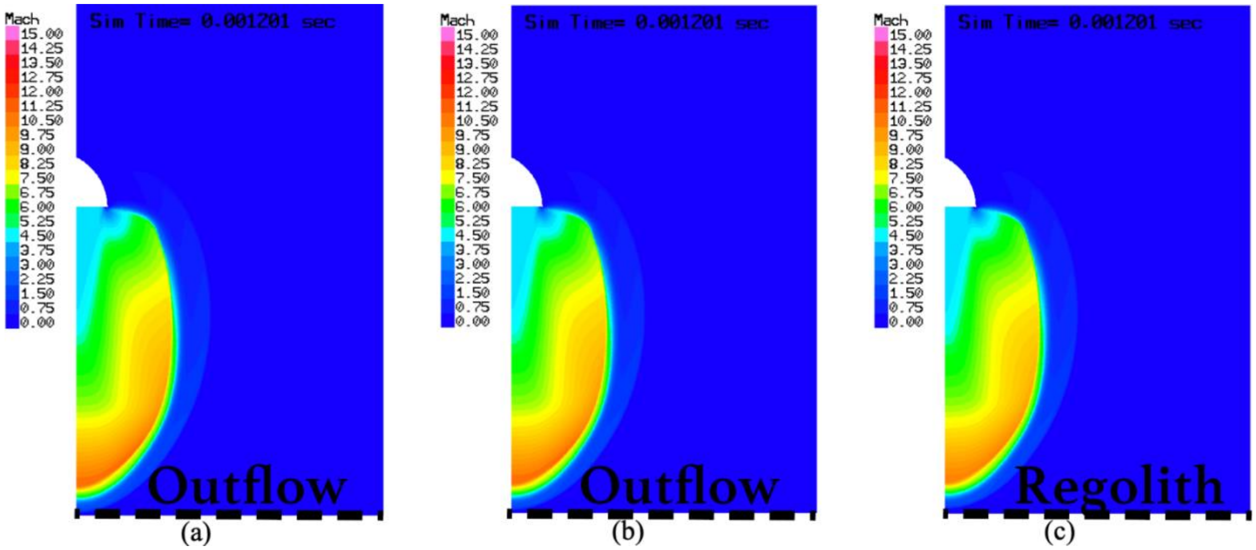

Fig. 1 Depiction of solution verification cases for the axisymmetric modeling capability: (a) gas-only *Loci/GGFS*, (b) gas-only *Loci/CHEM*, and (c) gas-granular *Loci/GGFS*

This series of test cases includes gas-only and gas-granular, axisymmetric CFD simulations using *Loci/GGFS* to verify the gas phase solution with respect to the gas-only solution obtained from *Loci/CHEM*. Each simulation includes the same nozzle geometry, initial conditions, and computational domain and boundary conditions, except for the gas-granular simulation with *Loci/GGFS*, where the domain is extended in the axial direction to include a surface of regolith below (refer to Fig. 2). Thus, gas-only, axisymmetric solutions from *Loci/GGFS* can be directly compared with those obtained from *Loci/CHEM*. The third case, gas-granular, axisymmetric *Loci/GGFS* simulation is then compared to the gas-only, axisymmetric *Loci/CHEM* solution only in the gas-only region of the domain where the solutions should be equivalent. At later flow times, PSI effects from an eroding regolith surface can alter the flowfield, as can be observed from Fig. 2, and therefore verification is performed using solutions only from early flow times.

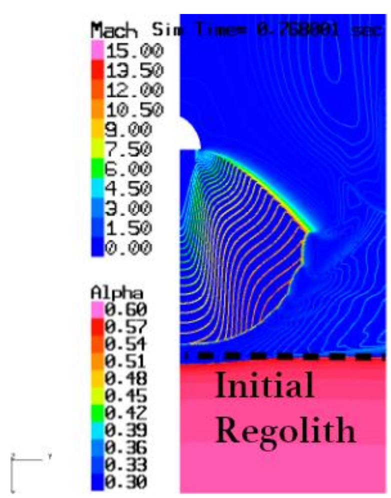

Fig. 2 Mach number and solid volume fraction contour plots for a late flow time in the gas-granular *Loci/GGFS* axisymmetric simulation

The nozzle geometry and inflow boundary conditions in each of the three cases are representative of those from Apollo LM, and a single-species air model is used to model the ambient Lunar environment and gas species exiting the nozzle (multiple-species modeling capability is verified in Section C). The conditions used for the cases are described in Table 1.

Table 1: Simulation Parameters

Simulation Parameter	Value
Species	Air
Gravity (m/s^2)	1.62
Ambient Pressure (Pa)	1
Ambient Temperature (K)	250
Nozzle exit diameter (m)	0.6
Nozzle Height above Surface (m)	3
Nozzle Inflow Pressure (Pa)	500
Nozzle Inflow Temperature (K)	500
Nozzle Inflow Velocity (m/s)	2000
Regolith dispersion (granular simulation only)	Mono-disperse
Regolith size (granular simulation only) (m)	1e-4

There are several gas-granular flow features that can be verified qualitatively using visual inspection of contour plots similar to those shown in Fig. 1 and animations of the various state variables like Mach number, pressure, temperature, and regolith volume fraction for the granular bed impingement simulation. These features include Mach profile expansion, pressure distribution across inflow boundary, and temperature increase in the boundary layer around the nozzle lip. For the granular bed impingement simulation several others also are available: granular material lateral movement/blow-out, granular material cratering, and gas pressure penetration into the granular bed. Many of these can be seen from the Mach number contour plots shown in Fig. 1, but a closer inspection (not shown here for conciseness) of temperature and pressure contours over simulated flow time reveals similar features and therefore verify the solutions qualitatively.

While visual inspection of contour plots and animations similar to those shown in Fig. 1 is useful to identify general trends and problems, it is not sufficient to quantitively evaluate the code-to-code differences. To accomplish this, a more detailed analysis using multiple line probes throughout the simulation spatially and temporally are compared between codes. This setup and an example of the type of comparisons made are shown in Fig. 3.

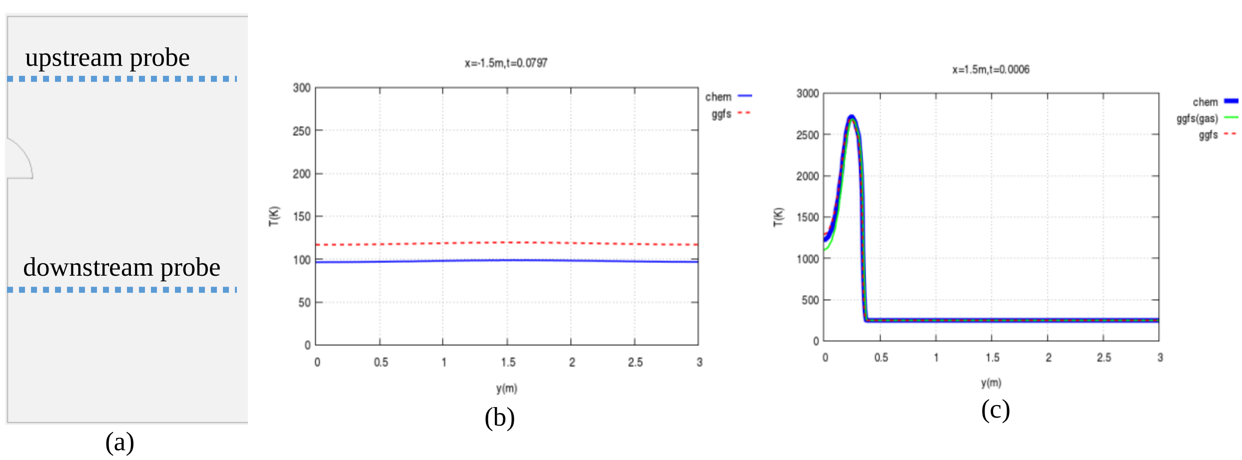

Fig. 3 Depiction of spatial and temporal analysis using lines of probes throughout the domain: (a) locations of two lines of probes in the domain, (b) gas-only *Loci/GGFS vs Loci/CHEM* temperature along upstream line of probes and (c) gas-only *Loci/GGFS vs Loci/CHEM* vs gas-granular *Loci/GGFS* temperature along downstream line of probes

Generally, the probes throughout the simulation show comparable or visually indistinguishable results. However, there are several locations that show noticeable (between 10% and 20%) differences in probe profiles over time. Figure 3 shows two of these locations that correspond to upstream of the nozzle in the ambient region and downstream of the nozzle. The temperature in the upstream line of probes is compared at a late flow time between the gas-phase only *Loci/CHEM* and *Loci/GGFS* simulations in Fig. 3(b). Temperature in this region of the domain shows the most discrepancy between the two solvers, with a difference of approximately 20 K at this flow time. The second region of noticeable discrepancy is along the downstream line of probes near the symmetry axis (y=0 m) at an early point in time when the plume is initially passing through. This discrepancy can be observed from Fig. 3(c), which shows the temperature along the downstream line of probes as obtained from *Loci/CHEM* and gas-phase only and gas-granular *Loci/GGFS* simulations. The gas-phase only and gas-granular *Loci/GGFS* temperatures lie on opposite sides of the *Loci/CHEM* solution near the symmetry axis but are in good agreement in both amplitude and phase with *Loci/CHEM* at the peak of the propagating wave. Thus, there is good agreement overall between *Loci/GGFS* and *Loci/CHEM* with at worst 20% difference in temperature ambient regions upstream of the nozzle and near the symmetry axis during the initial transient.

B. Overset Mesh/Moving Mesh Capability

Implementing an overset mesh/moving mesh capability adds additional physics to *Loci/GGFS* by allowing for the simulation of a landing vehicle during descent, including the transient PSI effects as the vehicle approaches the surface. In order to verify the implementation of this capability, a total of five simulations have been performed with the same geometry and similar inflow conditions and initial conditions as used in the simulations described in Section A for axisymmetric modeling: (1) gas-only, axisymmetric *Loci/GGFS* simulation of a representative Lunar lander plume with overset mesh with no movement, (2) gas-only, axisymmetric *Loci/CHEM* simulation of a representative Lunar lander plume with overset mesh with no movement, (3) gas-only, axisymmetric *Loci/GGFS* simulation of a representative Lunar lander plume with overset mesh with moving mesh, (4) gas-only, axisymmetric *Loci/CHEM* simulation of a representative Lunar lander plume with overset mesh with moving mesh, and (5) gas-granular, axisymmetric *Loci/GGFS* simulation of a representative Lunar lander plume with overset mesh with moving mesh and a regolith surface below. The only difference in inflow and initial conditions is the use of an equivalent single species gas mixture to model the Hydrazine combustion product gases from Apollo LM. See Fig. 4 below for a depiction of these five cases.

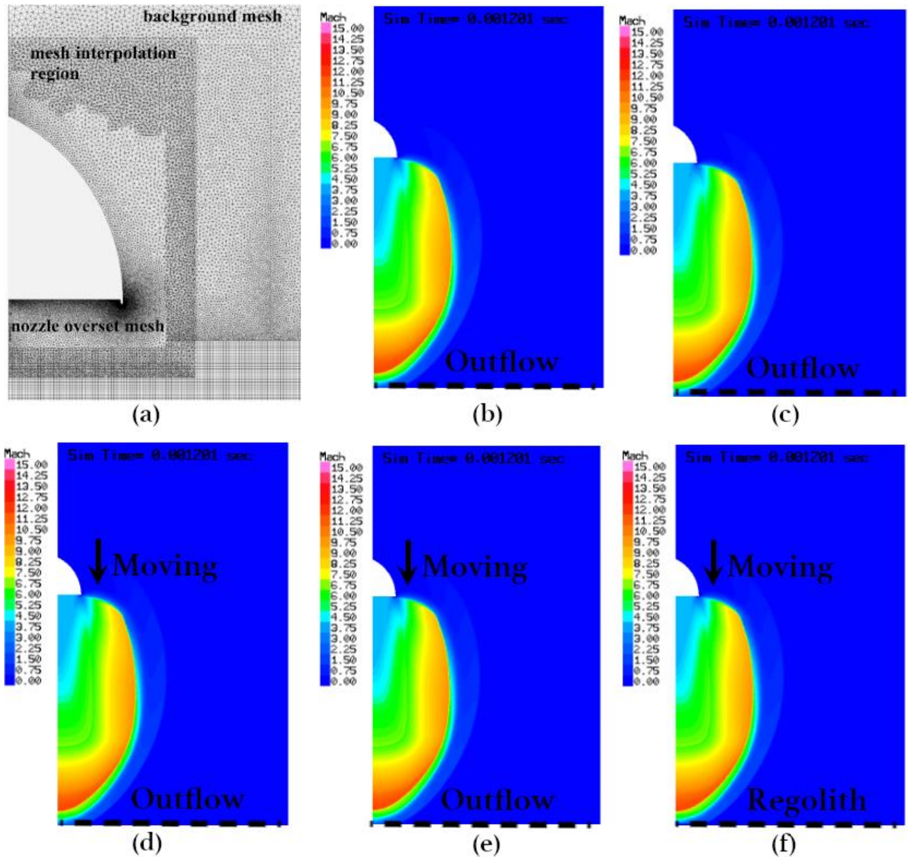

Fig. 4 Depiction of solution verification cases for the overset mesh/moving mesh capability: (a) background, nozzle overset, and interpolated regions of mesh (b) gas-only *Loci/GGFS* with no movement, (c) gas-only *Loci/CHEM* with no movement, (d) gas-only *Loci/GGFS* with moving mesh, (e) gas-only *Loci/CHEM* with moving mesh, and (f) gas-granular *Loci/GGFS* with regolith surface and moving mesh.

The progression of these solution verification cases is of increasing complexity. First, an overset mesh is generated as indicated in the boxed region around the nozzle in Fig. 4 above, and a velocity of zero is specified to keep the position fixed in space. Gas-only solutions are then obtained from both *Loci/GGFS* and *Loci/CHEM* for verification. Secondly, a velocity of 2 m/s in the +X direction (downwards) is specified for the moving mesh in order to verify the solution under conditions of a representative descent profile. Gas-only solutions are again obtained from *Loci/GGFS* and *Loci/CHEM* for comparison. Lastly, a regolith surface is added below the nozzle and the same moving mesh is used in a gas-granular *Loci/GGFS* simulation to verify the overset mesh/moving mesh capability under representative conditions of a Lunar lander approaching the surface. The gas-phase region of the gas-granular *Loci/GGFS* simulation is then verified against the gas-only simulation using *Loci/CHEM*. Mach number and temperature profiles will be compared between *Loci/GGFS* and *Loci/CHEM* next for each set of conditions.

The same qualitative verification of gas-granular flow features discussed in the previous section are performed here, with the additional verification of nozzle geometry descent rate for all moving mesh simulations. For conciseness, these features have been verified qualitatively, but detailed inspections are not provided. The more significant metrics used to quantify discrepancies in the simulations are shown in Fig. 5 for Mach number and temperature along lines of probes upstream of the nozzle, along the nozzle exit plane, and downstream of the nozzle, respectively.

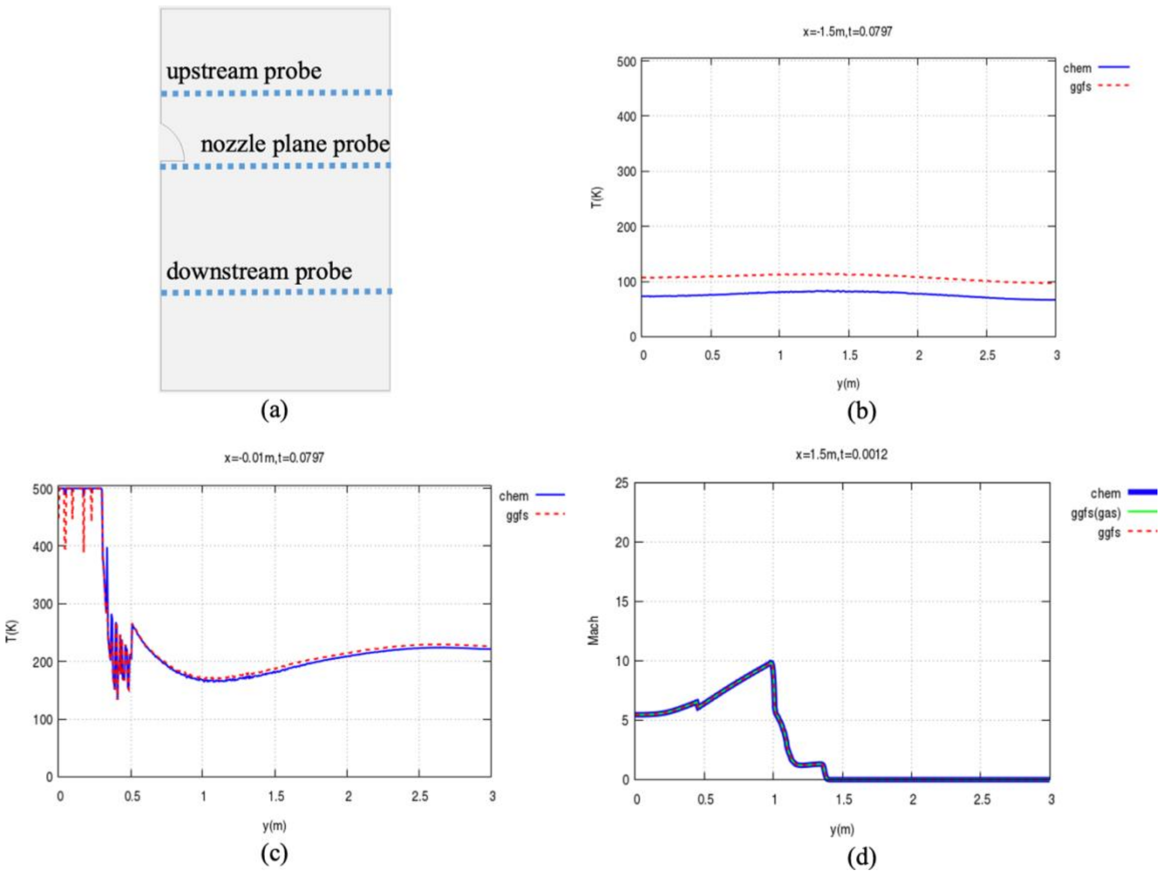

Fig. 5 Depiction of spatial and temporal analysis using lines of probes in the domain: (a) locations of lines of probes in the domain, (b) gas-only *Loci/GGFS vs Loci/CHEM* temperature along upstream line of probes, (c) gas-only *Loci/GGFS vs Loci/CHEM* temperature along nozzle exit plane, and (d) gas-only *Loci/GGFS vs Loci/CHEM* vs gas-granular *Loci/GGFS* Mach number along downstream line of probes

Figure 5(b) shows a similar temperature discrepancy that was seen in the previous section in the same ambient region upstream of the nozzle. A trend that is specific to the overset/moving mesh simulation is shown in Fig. 5(c), which depicts a jagged temperature profile near the nozzle exit. This is not seen in other simulations and is indicative of the importance of having a good overset-to-background mesh relationship so as to allow smooth interpolation between them. There are some discrepancies between *Loci/GGFS* and *Loci/CHEM* right at the nozzle, likely due to differences in interpolation. Mach number profiles along the downstream line of probes are shown in Fig. 5(d) between all three moving mesh simulations (*Loci/CHEM*, gas-phase only *Loci/GGFS*, and gas-granular *Loci/GGFS*) at an instant in time when the plume passes through. As can be observed from Fig. 5(d), each simulation is in good agreement at the downstream location. Overall, there is good agreement everywhere in the domain between each simulation, with slight discrepancies (spikes/jaggedness) in difficult to interpolate regions, and temperature differences of approximately 10% in the upstream ambient region.

C. Multiple-Species Modeling Capability

Implementing a multiple-species modeling capability adds additional physics to *Loci/GGFS* by allowing for the simulation of realistic gas mixtures and species transport. In order to verify the implementation of this capability, a total of three simulations have been performed with the same geometry, inflow conditions, and initial conditions as used in the simulations described in Section A for axisymmetric modeling: (1) gas-only, axisymmetric *Loci/GGFS* simulation of a representative Lunar lander plume with a two-species gas mixture, (2) gas-only, axisymmetric *Loci/CHEM* simulation of a representative Lunar lander plume with a two-species gas mixture, and (3) gas-granular, axisymmetric *Loci/GGFS* simulation of a representative Lunar lander plume with a two-species gas mixture and a regolith surface below (see Fig. 6 below for a depiction of these three cases).

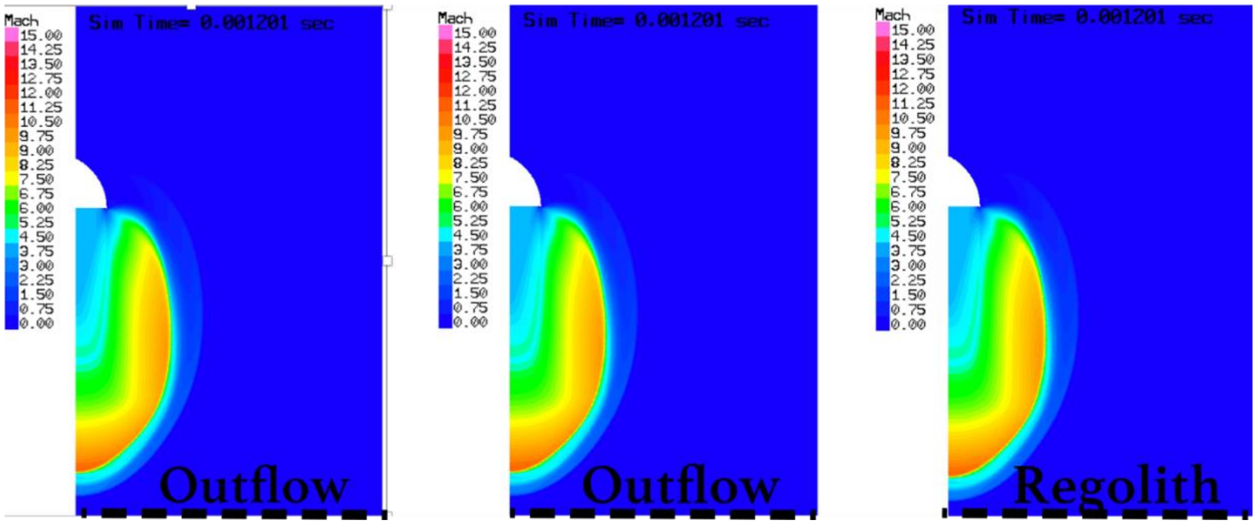

(a) (b) (c)

Fig. 6 Depiction of solution verification cases for the multi-species modeling capability: (a) gas-only *Loci/GGFS* with two-species gas mixture, (b) gas-only *Loci/CHEM* with two-species gas mixture, and (c) gas-granular *Loci/GGFS* with two-species gas mixture and a regolith surface

The two-species gas mixture used for solution verification of the multi-species capability is comprised of the same, equivalent gas species from the nozzle flow discussed in the previous section plus an additional gas species representing the ambient, Lunar environment, CO_2. Thus, the inflow condition from the nozzle is specified with 100% concentration of the equivalent gas species, and the entire computational domain is initialized with 100% CO_2. As with the other two capabilities described in Sections A and B, the gas-only solutions from *Loci/GGFS* are compared with those from *Loci/CHEM*, and the gas-phase region of the gas-granular *Loci/GGFS* simulation is then verified against the gas-only simulation using *Loci/CHEM*. Gas species volume fraction contours and temperatures will be compared between *Loci/GGFS* and *Loci/CHEM* next for each set of conditions. The same qualitative verification described in Section A all apply here as well as one additional verification to ensure the simulated nozzle inflow and ambient regions result in the anticipated volume fractions of equivalent gas and CO_2, respectively. This additional verification is shown in Fig. 7.

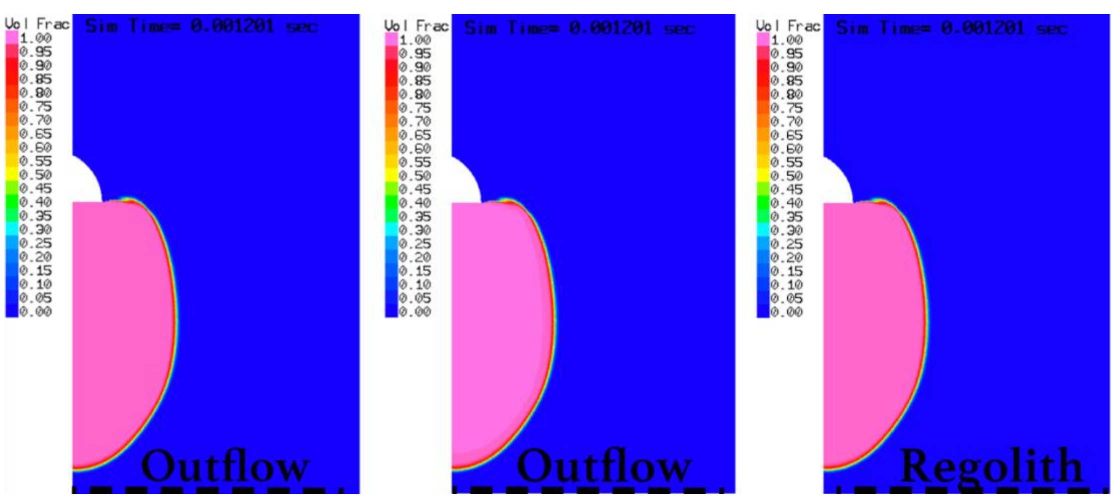

(a) (b) (c)

Fig. 7 Depiction of solution verification cases for the multi-species modeling capability: (a) gas-only *Loci/GGFS* with two-species gas mixture, (b) gas-only *Loci/CHEM* with two-species gas mixture, and (c) gas-granular *Loci/GGFS* with two-species gas mixture

Figure 7 shows that each case is providing 100% Apollo LM equivalent species as inflow to the nozzle while maintaining 100% CO_2 in the ambient region and thus provides a verification of the multiple-species gas mixture implementation into *Loci/GGFS*. The other gas-granular flow features are also verified, but again are not shown outside of what is available in Fig. 6 for conciseness. The more significant line probes used to quantify specific discrepancies in the simulations are shown in Fig. 8.

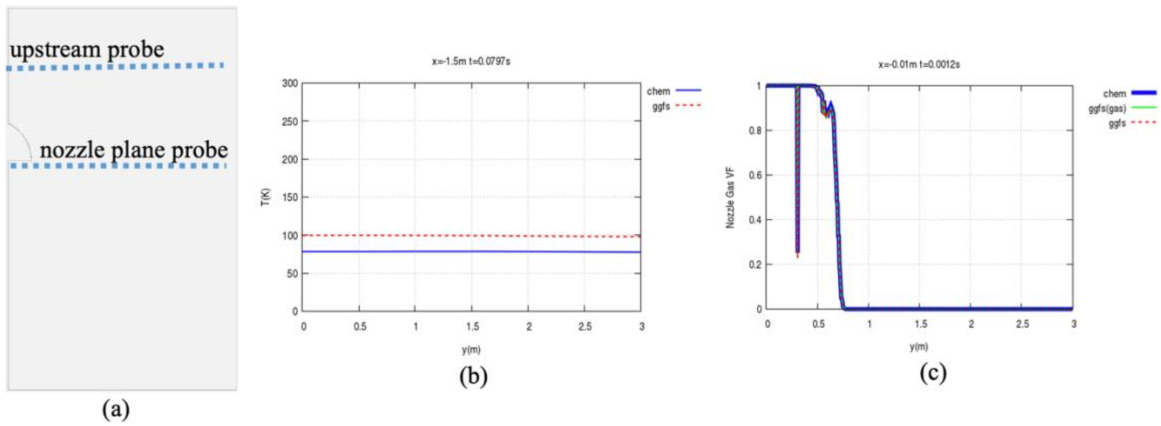

Fig. 8 Depiction of spatial and temporal analysis using probe lines throughout the domain: (a) locations of lines of probes in the domain, (b) gas-only *Loci/GGFS vs Loci/CHEM* temperatures along upstream line of probes and (c) gas-only *Loci/GGFS vs Loci/CHEM* vs gas-granular *Loci/GGFS* volume fractions along nozzle inflow plane

As with the other two capabilities verified in the previous sections, there is generally good agreement between the *Loci/CHEM* and *Loci/GGFS* simulations with the largest discrepancy occurring at late simulated flow times in the ambient region upstream of the nozzle. This discrepancy can be observed from Fig. 8(b). Fig. 8(c) compares the volume fractions of the nozzle gas from each of the three simulations along the nozzle inflow plane at an early flow time. The volume fractions compare well, with the largest discrepancy located at the nozzle lip approximately 0.3m in the y-direction.

IV. Demonstration of Cratering Simulation Capability

A demonstration of the current capabilities is provided in this section with respect to a 3D cratering simulation of Apollo LM at an altitude of 5 meter of the nozzle exit above the Lunar surface. The LM nozzle has an exit diameter of 1.457m. By simulating cratering from Apollo LM, current capabilities for a set of realistic conditions can be assessed with respect to a representative human lander landing on the Moon. The *Loci/GGFS* tool is used to simulate the 3D geometry shown in Fig. 9 below. A regolith layer 3m deep below the surface is comprised of monodisperse spherical particles with a diameter of 100 microns.

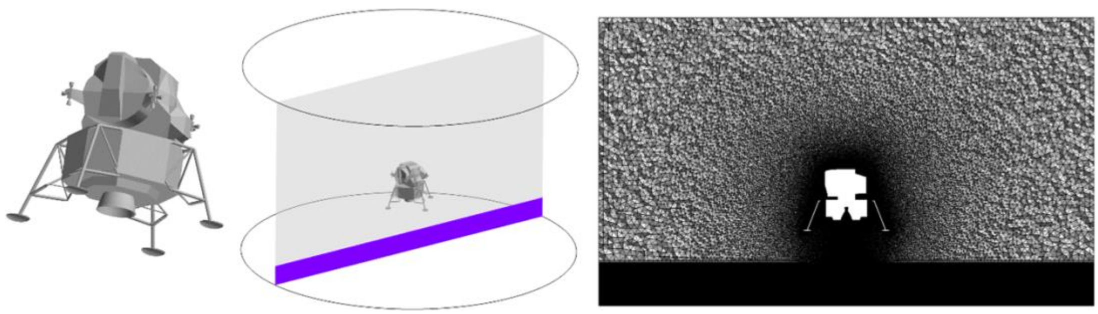

Fig. 9 Computational geometry in *Loci/GGFS* cratering simulation of Apollo LM at 5m altitude

The simulation is performed with the entire domain set to an initial ambient pressure of 0.1 Pa, a relatively low but non-zero pressure to demonstrate the ability of the currently continuum-based solver to perform in the vacuum environment on the Moon. The plume flow is composed of a Hydrazine combustion product surrogate gas and initiated from the engine chamber inflow conditions at 23 psi chamber pressure. This corresponds to Apollo LM terminal descent thrust levels of approximately 2200 lbf. The plume flow is initiated impulsively through the nozzle into the initial quiescent domain and impinges on the regolith surface to quickly progress into a fully developed plume flow field. At the low elevation of 5m, the plume flow expands to a supersonic outflow in both outward and upward directions, as shown in Fig. 10. Note how the plume flow escapes from the stagnation region forming inside the developing crater in an outward supersonic, high shear flow pattern along the crater walls and the lunar surface as the main erosion mechanism.

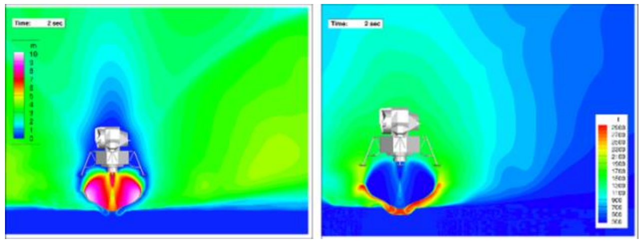

Fig. 10 Cross Section of Apollo LM flow field at 5m altitude showing Mach number and Temperature. Notice high shear, supersonic flow escaping from post-shock stagnation region along crater surface

The resulting particle ejecta patterns can be observed from contours of solid volume fraction shown in Fig. 11 below. As the plume initially impinges on the lunar surface below, regolith is lofted and slowly ascends upward with the farfield plume flow. Once the quasi-steady plume field has settled, the ground regolith begins to be eroded steadily and is ejected radially outwards at low angles in the 5- to 10-degree range and with a streaking pattern similar to those observed in actual landing footage. The crater forms under the central portions of the plume where the highest impingement pressure and shear layer levels occur.

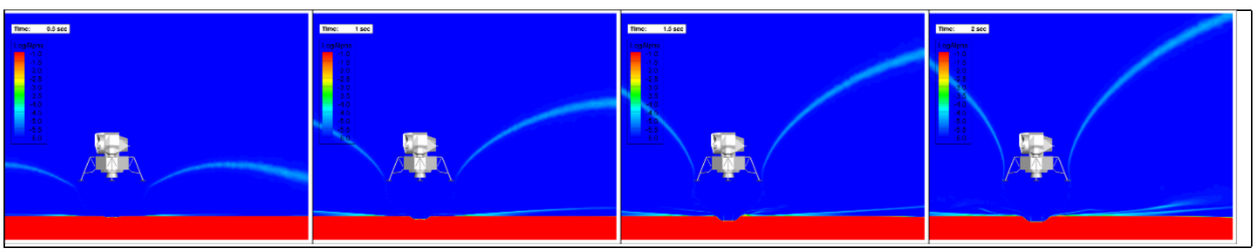

Fig. 11 Contours of solid volume fraction indicating formation of crater and shallow angle near-surface ejecta sheets, with ascending particle cloud resulting from impulsive plume start-up and impingement

A total of two seconds of flow time was simulated, resulting in a relatively wide but shallow crater of approximately 0.75m depth and diameter approaching 4.0m, as shown in Fig. 12. Such crater dimensions are obviously much larger than actual craters observed for the actual lunar regolith composition. The regolith simulant model applied here used a simple mono-disperse spherical shape model, albeit with a more realistic internal friction angle of 45 degrees. *Loci/GGFS* is designed to perform particle composition modeling of more realistic irregular, jagged, non-spherical particle shapes and poly-disperse mixtures composed of a wide range of particle sizes. This more realistic particle phase modeling will be applied in follow-on work to improve the initial demonstration results reported here.

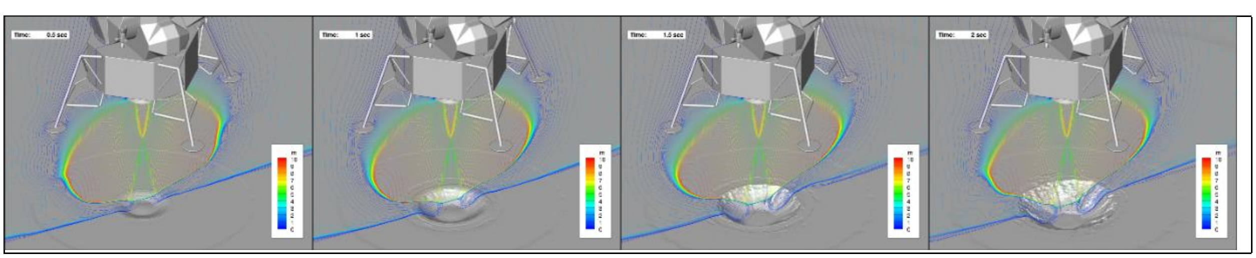

Fig. 12 Crater profile from 3D *Loci/GGFS* simulations of Apollo LM at various times up to two seconds

The purpose of the current simulation is to demonstrate the ability of *Loci/GGFS* to perform practical, full resolution, 3D, production level simulations for a representative Lunar lander with high Mach plume flow expansion under Lunar, near-vacuum external conditions. The accuracy of cratering predictions under relevant conditions is to be assessed with respect to validation cases, and this is the focus of the next section.

V. Validation Analyses of Surface Cratering in Martian and Lunar-Like Environments

This section provides an overview and brief status of three validation analyses of surface cratering performed in Martian and Lunar-like environments: (1) subsonic flow in a Martian-like environment,[5] (2) PFGT1 Martian-like case, and (3) PFGT1 Lunar-like case. Crater depth as a function of time is compared between *Loci/GGFS* and experimental data[**] in Metzger's subsonic flow test at PAL[5] in Section A. Since the PFGT1 test data were not available at the time this paper was written, the validation analyses indicated in Sections B and C below consist only of cratering results obtained from the pre-test simulations.

A. Subsonic Flow in Martian-like Environment

The subsonic flow test in a Martian-like environment refers to one of the test series performed by Metzger at the Planetary Aeolian Lab (PAL) in 2016 at a vacuum chamber pressure of 9.8 Torr (1300 Pa).[5] This test was performed using subsonic flow exiting a pipe and with a test bin filled with Jetty Park Beach Sand. The test bin is outfitted with a splitter plate that is aligned with the center of the pipe such that half of the pipe flow enters the test bin and half of the pipe flow is directed out of the test bin (see Fig. 13 below for a schematic of the test). Other conditions of the test, including geometric dimensions of the test, regolith properties, and flow properties are provided next.

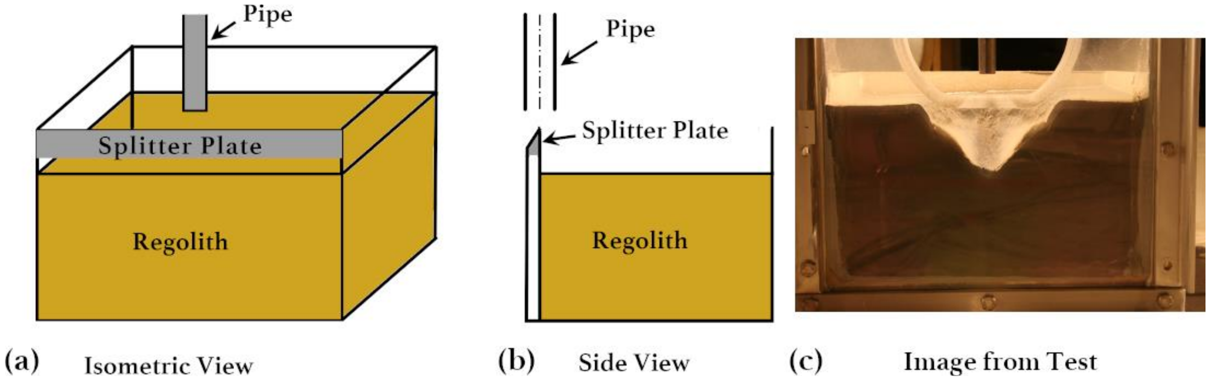

Fig. 13 Test setup of Metzger's subsonic flow test at PAL[5]: (a) schematic from isometric view, (b) schematic from side view, and (c) image of front view from test

A straight, circular pipe with an inner diameter of 0.37 in is positioned 1 in above the top of the splitter plate and aligned such that half the flow is directed into the test bin and half is directed out of the test bin. The test bin itself is 24 cm x 20 cm x 18.5 cm, with a splitter plate that is 3/8 in thick and 1/2 in long. The regolith is Jetty Park Beach Sand, which has a broad size distribution from 38 microns to 1400 microns. The mean diameter based on the mass distribution is 353 microns. The density of a single sand particle is 2610 kg/m^3. Nitrogen gas at 288 K flowed through the pipe with an exit velocity of 138.5 m/s and a mass flow rate of 8.82 g/min. The vacuum chamber pressure was 9.8 Torr. Next, the computational setup for the *Loci/GGFS* simulation is described.

The *Loci/GGFS* cratering simulation is performed with an axisymmetric model about the centerline of the pipe. Thus, the effects of the splitter plate on the flow and crater evolution are not modeled. The monodisperse spheres model is used, with the particle diameter specified at the mean particle diameter of 353 microns. The initial packing of the soil corresponds to a settled soil with a maximum packing factor of 0.63 for spheres, and therefore there is an initial gradient of solid volume fraction with increased soil depth at the start of the simulation. An internal angle of

[**]Experimental data obtained from private communication with Philip Metzger.

friction value of 28 deg. is specified, corresponding to a theoretical value for spheres. A diagram of the computational domain used in the *Loci/GGFS* simulation is provided in Fig. 14.

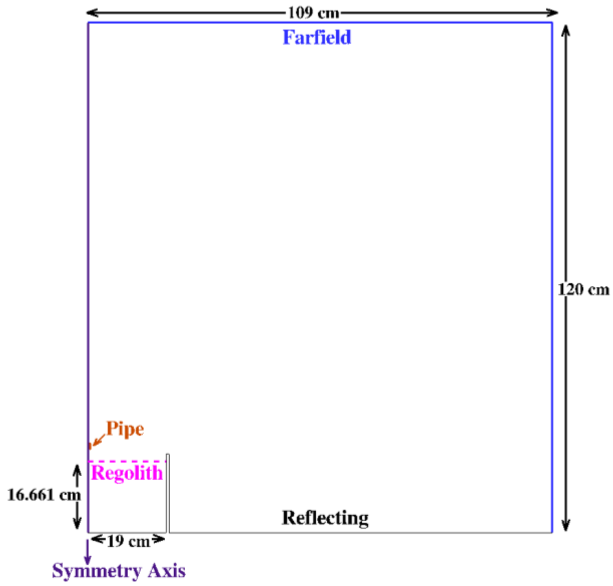

Fig. 14 Axisymmetric computational domain used in *Loci/GGFS* simulations of Metzger's[5] subsonic flow test at PAL

The flow of N_2 through the pipe was modeled at full flow rate in the simulations, effectively modeling an impulsive start. As the gas flow impinges on the regolith surface below, it begins to erode the surface and form a crater. This crater evolution process is shown in Fig. 15 for several instances in time from the *Loci/GGFS* simulation. The jet of N_2 gas is observed to be redirected at nearly a 45 deg. angle as a small crater begins to form at a time of 0.02 s. By a flow time of 0.15 s in the simulation, regolith that had been eroded from the surface is being entrained back towards the pipe exit. The gas velocity magnitude contours also indicate the inward-directed flow, and the regolith begins to obstruct the gas flow exiting the pipe. After 0.18 s, the lofted regolith is beginning to fall back into the crater, starting a recirculation process that impedes further crater growth. The recirculation process continues, and a similar crater shape and entrained regolith in the path of the gas jet is observed in the simulations at a time of 0.4 s. The data obtained from the experiment are maximum crater depth measurements taken along the splitter plate as a function of time, and this data will be used for validation of the cratering predictions from *Loci/GGFS*.

Maximum crater depth as a function of time is compared in Fig. 16 between *Loci/GGFS* and experimental measurements. A similar slope in the crater depth is initially observed between *Loci/GGFS* and experimental measurements, albeit offset with *Loci/GGFS* increasing in depth at earlier times. This offset is likely due to a combination of the impulsive start used in the simulation and the start time reported in the test, which was based on first observations of surface erosion. As described previously, the regolith begins to recirculate in the path of the gas jet, and oscillations in crater depth are evident after approximately 0.15 s. This process is affected by the splitter plate, as evident from pathfinder 3D simulations with the splitter plate that will be discussed next. The crater then begins to asymptote to approximately 1.5 cm in the simulation, whereas the crater in the test continues to grow in depth to approximately 3 cm after 10 s. The crater depths are shown for the *Loci/GGFS* simulation and experimental measurements in Fig. 16(a) and Fig. 16(b), for time scales of 1 s and 10 s, respectively.

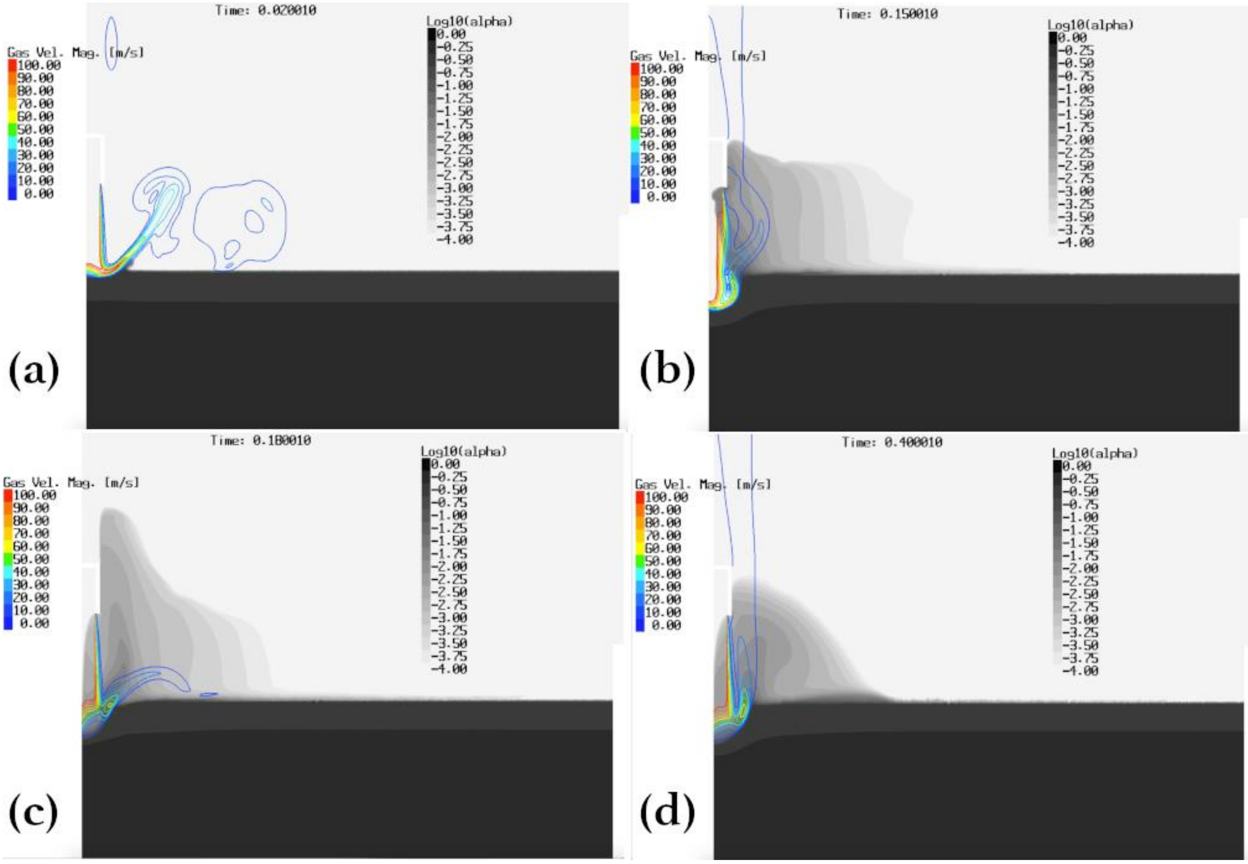

Fig. 15 Contours of gas velocity magnitude and $\log_{10}$ of solid volume fraction from *Loci/GGFS* simulation at flow times of (a) 0.02 s, (b) 0.15 s, (c) 0.18 s, and (d) 0.40 s

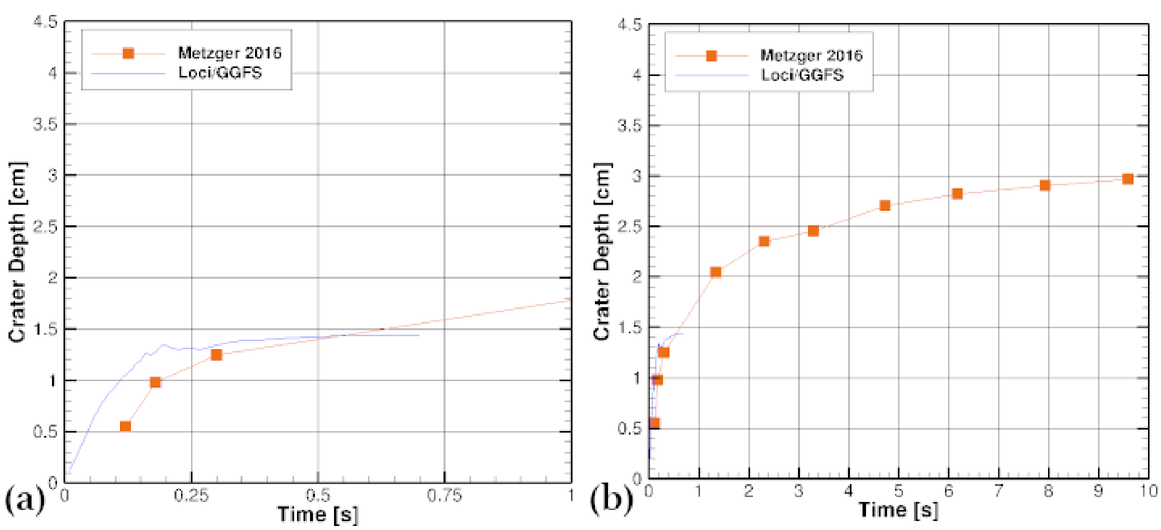

Fig. 16 Comparison of crater depth Vs. time between *Loci/GGFS* and experimental measurements at time scales of (a) 1 s and (b) 10 s

As part of the predictive tool maturation process, the full 3D geometry including the splitter plate has been modeled with *Loci/GGFS*, and a temporal evolution of the crater, ejecta, and jet flow structure can be observed from Fig. 17.

Three dimensional features are clearly visible from Fig. 17, including a piling of soil against the splitter plate, a noncircular crater that is wider than it is long, and gas flow and ejecta patterns that are streak-like and non-uniform around the crater circumference. As mentioned previously, the regolith from the 3D simulation is not observed to recirculate back into the crater as observed from the axisymmetric simulation. This demonstrates the current capability of *Loci/GGFS* to model 3D geometries with a splitter plate and its need in future validations along with realistic soil models.

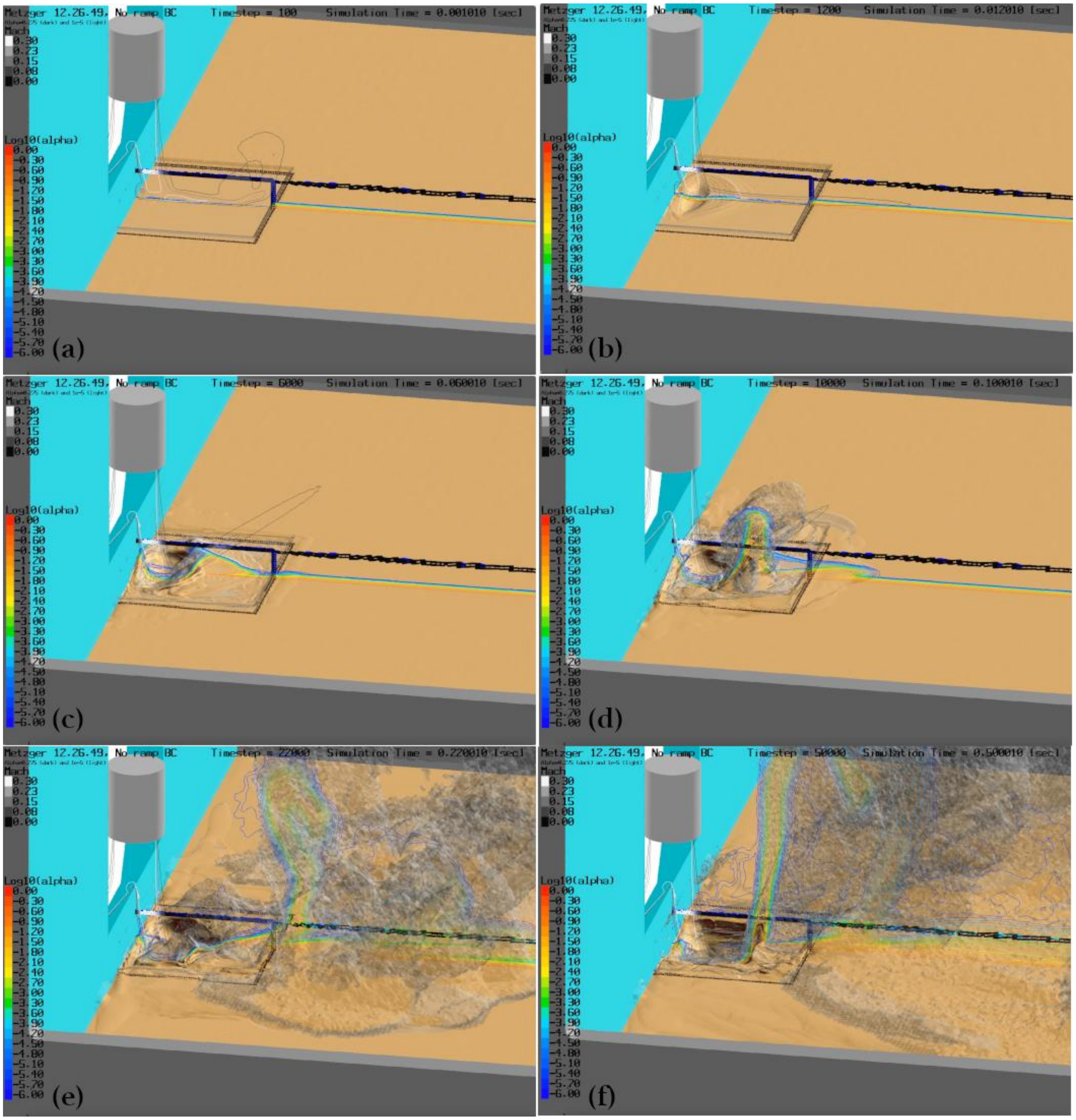

Fig. 17 Contours of Mach number and solid volume fraction from 3D *Loci/GGFS* simulations at times of: (a) 0 s, (b) 0.012 s, (c) 0.06 s, (d) 0.1 s, (e) 0.22 s, and (f) 0.5 s

B. Physics Focused Ground Test 1 Martian-like Case

Two pre-test simulations are performed ahead of the PFGT1 test series as part of the GCD program, one with a Martian-like environment and the other with a Lunar-like environment. This section pertains to the Martian-like environment case. The geometry of the test is shown in Fig. 18 with respect to a computer aided design model and a top-down view from the test. A similar test setup including a splitter plate is used as shown previously for the test at PAL,[5] but PFGT1 tests use a Mach 5.3 supersonic nozzle and lower vacuum chamber pressures.

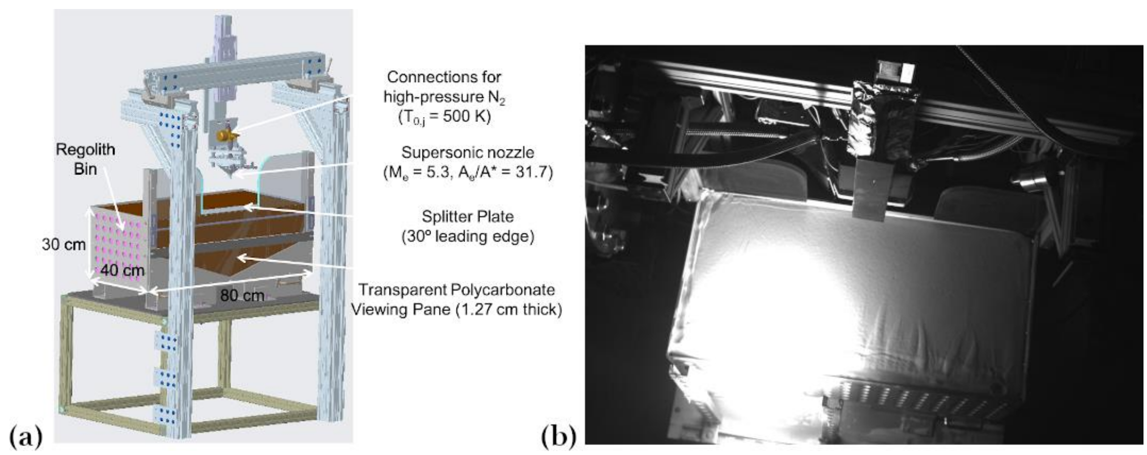

Fig. 18 Geometry of PFGT1 test setup: (a) computer aided design drawing and (b) top-down image from test

The computational model is axisymmetric with the symmetry axis aligned with the centerline of the nozzle. The computational model domain and a magnified view of the region near the nozzle are shown in Fig. 19, respectively. Farfield boundary conditions are specified on the outer boundaries of the computational domain with the ambient conditions of the test, vacuum pressure of 267 Pa and a temperature of 300 K. The simulation was started with initial conditions set to quiescent and the gas/soil interface set at the location indicated by the dashed line in above, 5.6 cm below the nozzle exit. The regolith is modeled as monodisperse spheres with a diameter of 150 microns and particle density of 2610 kg/m^3. The flow of heated, 500 K, N_2 gas through the Mach 5.3 supersonic nozzle was activated at the start of the simulation with an inflow boundary condition specified at the nozzle throat. This inflow boundary condition varied over time with a ramping profile as shown in Fig. 20 with respect to mass flow rate as a function of time.

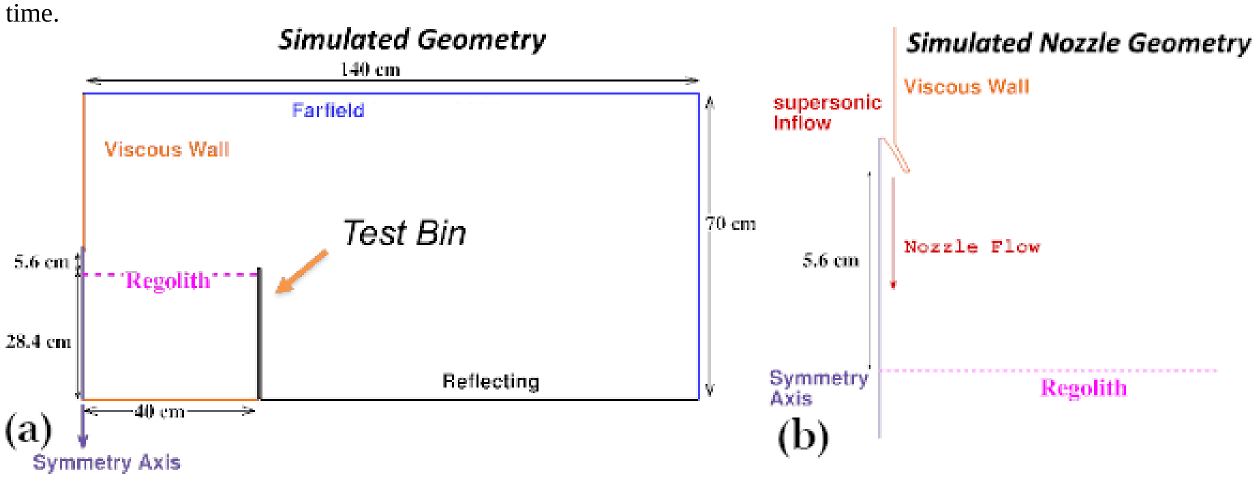

Fig. 19 Illustration of computational domain and associated boundary conditions for axisymmetric simulations of PFGT1 Martian-like and Lunar-like cases, (a) entire computational domain and (b) computational domain near nozzle

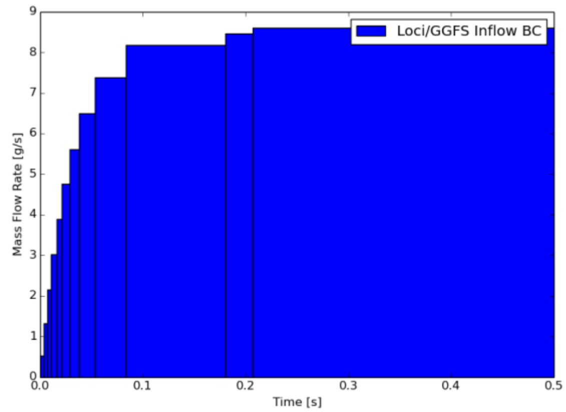

Fig. 20 Inflow nozzle mass flow rate boundary condition for PFGT1 Martian-like case

Contours of plume Mach number and solid volume fractions are shown in Fig. 21 at various instances in time from a view that includes the entire width and depth of the regolith bin. Note that this is an axisymmetric simulation, and that the solution on the left half of the images in Fig. 21 are mirrored. A crater begins to form within 0.04 s that is deepest in an annular region about the nozzle centerline. An initial splash of soil is observed that propagates radially outwards over time. The cratering process is relatively violent with a pulsing behavior within the crater that expels significant amounts of dense ejecta, as observed at a time of 0.4 s in Fig. 21. Numerous, small craters begin to form all over the test bin as dense streams of ejecta fall and impact the undisturbed regolith surface below. These smaller craters are evident at a time of 0.65 s in Fig. 21.

The maximum crater depth is evaluated as a function of time from the simulation and reported graphically in Fig. 22. The crater depth grows to approximately 7 cm at 0.2 s but then begins to decrease as the pulsing behavior begins. Oscillations in crater depth are observable in Fig. 22, but the running average of crater depth over time indicates that the crater depth is leveling out after approximately 0.4 s. These cratering characteristics and crater size predictions will be compared with test data for validation after the data becomes available.

A full 3D model geometry including the splitter plate has been simulated for PFGT1 under Martian-like conditions similar to the 3D simulation of the subsonic flow test at PAL.[5] A temporal evolution of the crater and plume structures are shown in Fig. 23 for the 3D *Loci/GGFS* simulations. The supersonic plume impinges on the regolith surface below and excavates a deeper crater in the annular region where the supersonic flow impinges. A cellular structure along the circumference of the crater becomes apparent over time and with regolith piling against the splitter plate. This demonstrates the 3D nature of the PSI effects and the need for maturing the predictive tool with 3D modeling capability. Future validation analyses will utilize the 3D modeling capabilities demonstrated herein.

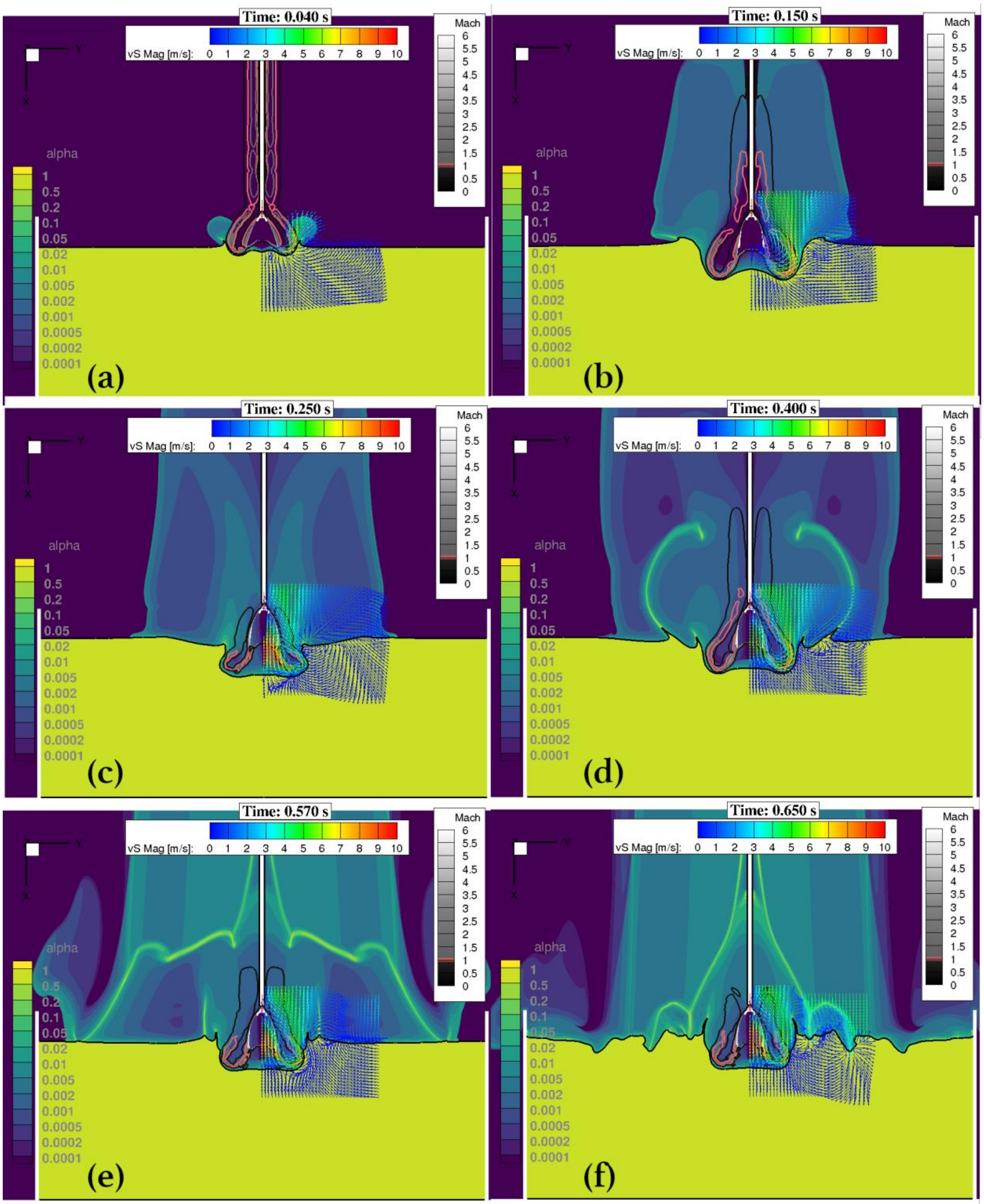

Fig. 21 Surface cratering results from *Loci/GGFS* simulation at times of (a) 0.04 s, (b) 0.15 s, (c) 0.25 s, (d) 0.4 s, (e) 0.57 s, and (f) 0.65 s

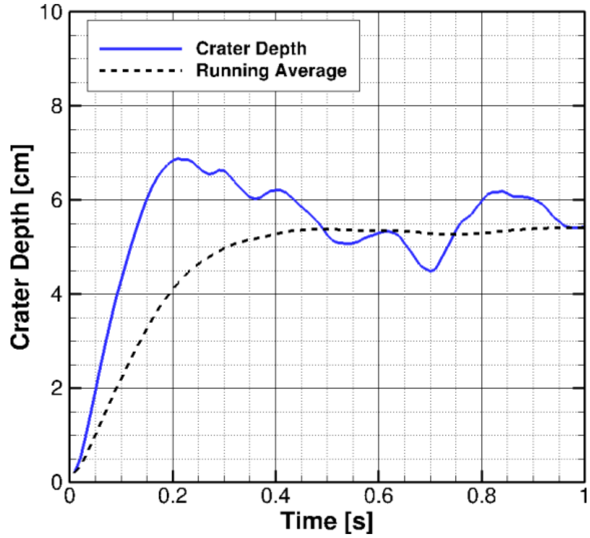

Fig. 22 Crater depth as a function of time from *Loci/GGFS* simulation of PFGT1 Martian-like case

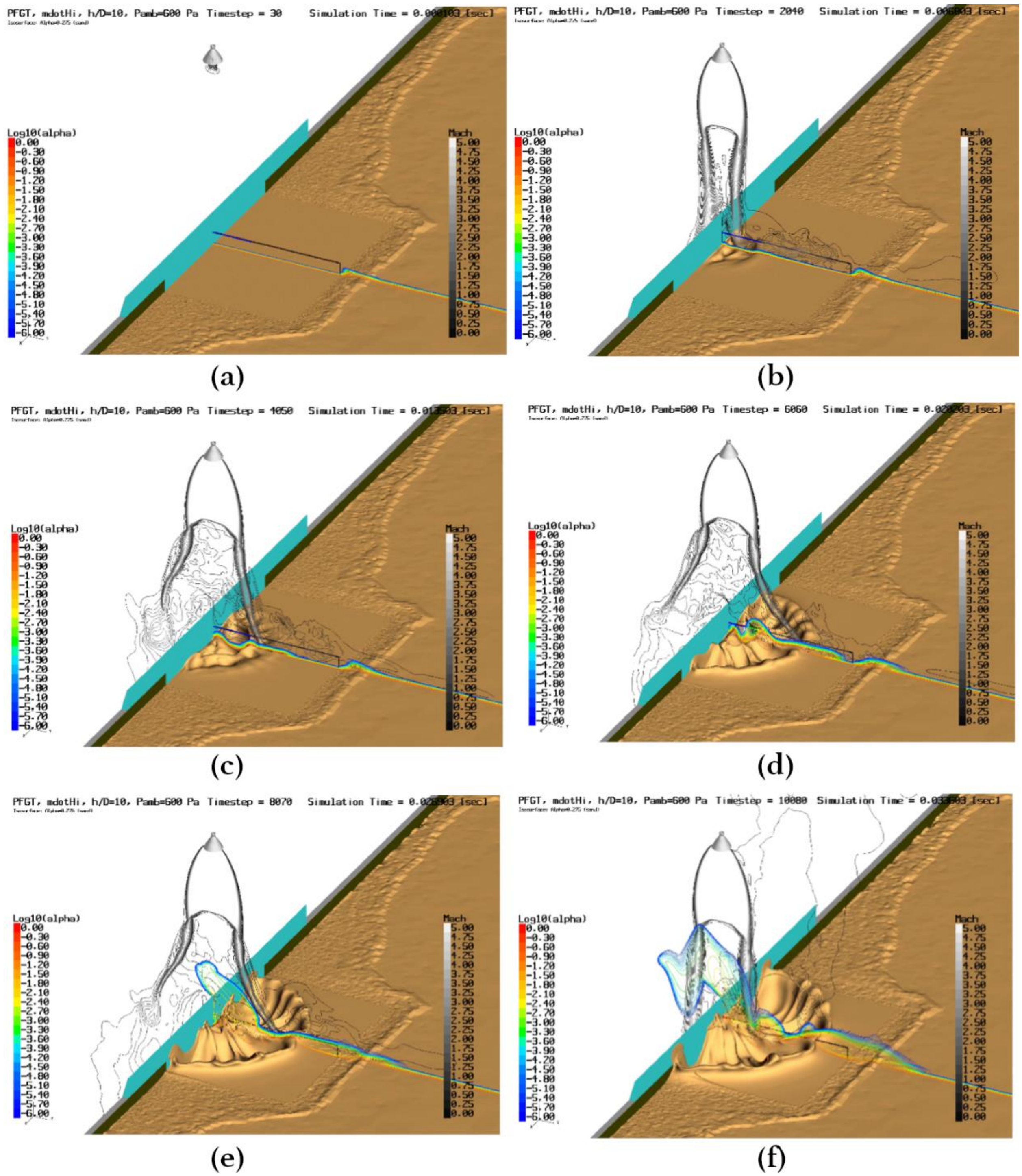

Fig. 23 Crater profile from 3D *Loci/GGFS* simulations of PFGT1 under Martian-like conditions

C. Physics Focused Ground Test 1 Lunar-like Case

The second of two, pre-test simulations performed ahead of the PFGT1 test series is presented in this section. The computational model geometry and domain is the same as shown in in the previous section, but the ambient conditions and nozzle flow conditions differ. A vacuum chamber pressure of 10 Pa is applied at the farfield boundaries, corresponding to a Lunar-like environment, and the nozzle mass flow rate ramps up over time to 0.32 g/s, where the transient mass flow rate is scaled by a constant factor from that of the Martian-like case in the previous section. The same, 150 micron spherical particles are modeled for the regolith as in the Martian-like case.

Contours of plume Mach number and solid volume fractions are shown in Fig. 24 at various instances in time from a view that includes the entire width and depth of the regolith bin. Note that this is an axisymmetric simulation, and that the solution on the left half of the images in Fig. 24 are mirrored. A crater begins to form early on that is deepest in an annular region about the nozzle centerline. As with the Martian-like environment case, regolith can be seen moving up out of the crater and propagating outwards radially. However, the crater size is significantly smaller than that of the Martian-like environment case shown in the previous section. The plume continues to erode the regolith surface below and eject regolith material upwards and outwards, without the recirculation within the crater observed previously for the Martian-like case.

The maximum crater depth as a function of time is reported graphically in Fig. 25. An overshoot in crater depth is observed during the first 0.2 s, before reaching a nearly constant crater depth after 0.35 s. This is a similar behavior as observed for the Martian-like environment case, albeit with greatly reduced oscillations and reduced crater depths. The crater depth after 1 s is approximately 0.8 cm. These cratering characteristics and crater size predictions will be compared with test data for validation after the data becomes available.

Both pre-test simulations assumed symmetry about the nozzle axis, but 3D effects with the splitter plate are present that need to be included in future validation analyses. These pre-test simulations provide an initial assessment of cratering predictions in both Martian-like and Lunar-like environments using current modeling capabilities, but additional PFGT1 tests will be revisited in future work using the 3D modeling capabilities already demonstrated along with realistic soil models that incorporates non-spherical, polydisperse particle effects.

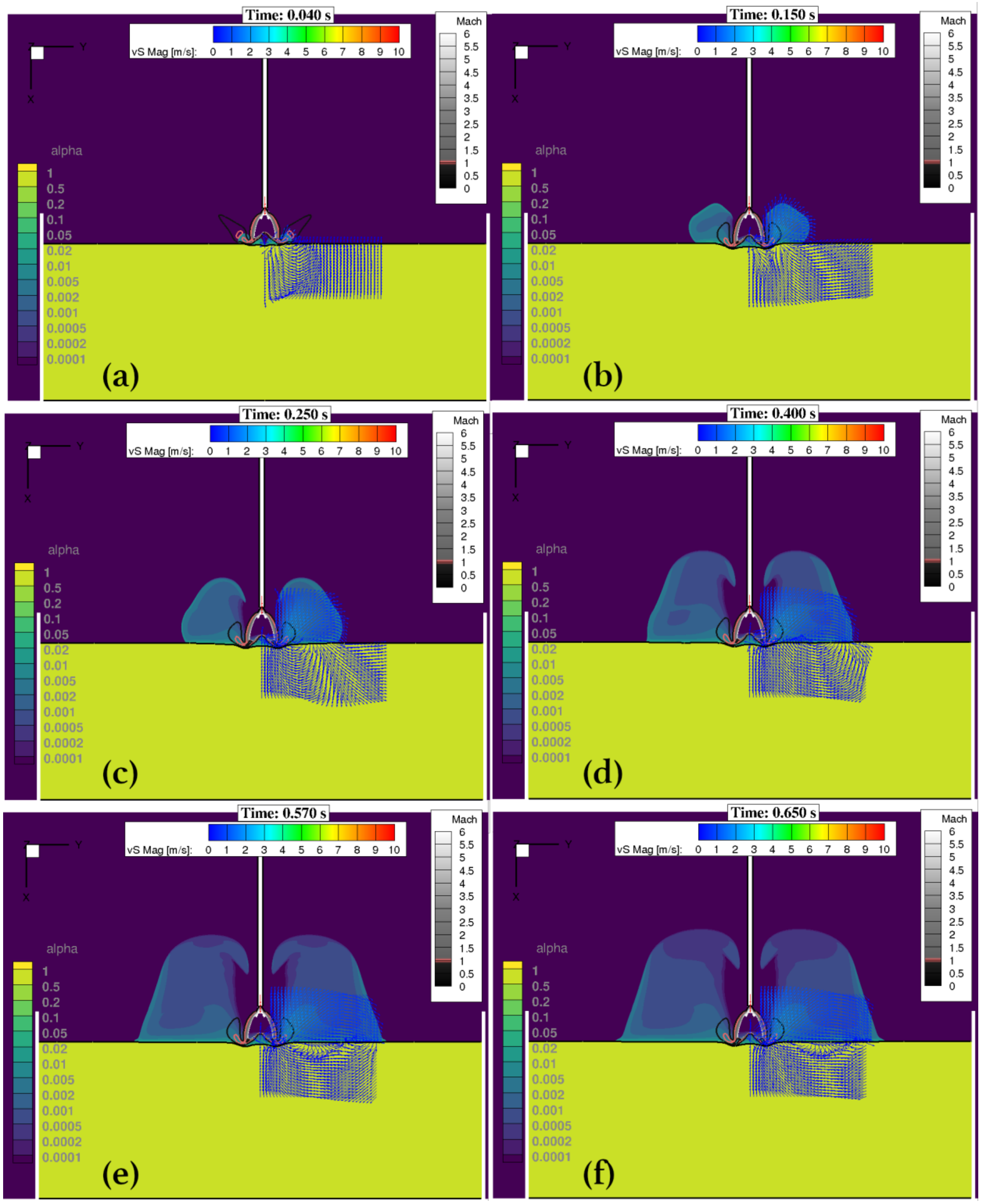

Fig. 24 Surface cratering results from *Loci/GGFS* simulation at times of (a) 0.04 s, (b) 0.15 s, (c) 0.25 s, (d) 0.4 s, (e) 0.57 s, and (f) 0.65 s

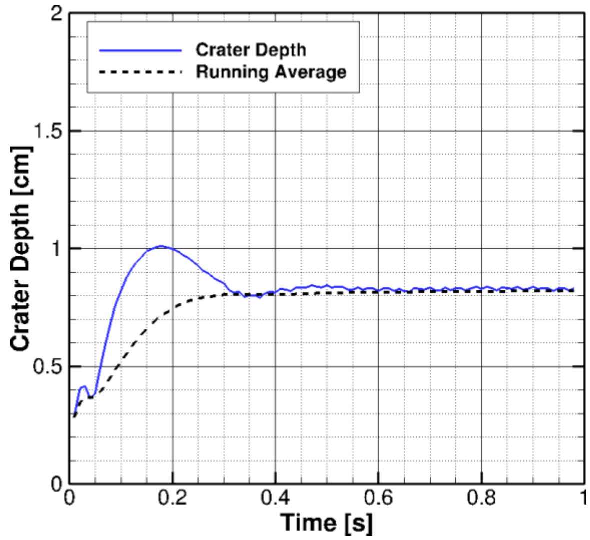

Fig. 25 Crater depth as a function of time from *Loci/GGFS* simulation of PFGT1 Lunar-like case

VI. Conclusion

Plume surface interaction induced environments is an important subject of study in order to address the risks it poses to landing vehicle, its crew, and nearby assets. The predictive simulation capabilities developed through the Game Changing Development Program are the first of its kind to fulfill this need on upcoming NASA missions to the Moon and Mars. The statuses of predictive simulation capability development presented in this paper provide a perspective into the scope and depth of analyses performed on one aspect of developing an accurate and reliable prediction capability for plume surface interactions, cratering and ejecta in continuum/rarefied flows. Each new implementation into the predictive simulation tool, *Loci/GGFS*, is verified, the tool is matured and tested for production readiness, and validated against multiple data sets in environments relevant to the intended extra-terrestrial landing applications. This development process will continue as capabilities are added and matured, such as polydisperse, irregular particle modeling and coupling with a Boltzmann solver to capture rarefied flow effects.

Acknowledgments

This study was performed under the Task Order ER42.12.01.EDLS.PSI.01 of the ESSCA Contract 80MSFC18C0011. The useful discussions and validation data provided by Philip Metzger of University of Central Florida are greatly appreciated.

References

[1] Gale, M., Buettner, K., Mehta, R., Liever, P. A., and Curtis, J., "Gas-Granular Flow Solver for Plume Surface Interaction and Cratering Simulations," AIAA 2017-4503. *23rd AIAA Computational Fluid Dynamics Conference*, June 2017. doi: 10.2514/6.2017-4503

[2] Luke, E. A., Tong, X., Wu, J., Cinnella, P., Chamberlain, R., and Walters, K., "CHEM 4.0: A Finite-Rate Viscous Chemistry Solver – The User Guide," September 2016.

[3] Velura, S. P., "Code Verification and Numerical Accuracy Assessment for Finite Volume CFD Codes," Ph.D. Dissertation, Virginia Polytechnic Institute and State University, Blacksburg, VA, 2010.

[4] West, J. S., Strutzenberg, L. L., Putnam, G. C., Liever, P. A., and Williams, B. R., "Development of Modeling Capabilities for Launch Pad Acoustics and Ignition Transient Environment Prediction," AIAA 2012-2094. *18th AIAA/CEAS Aeroacoustics Conference (33rd AIAA Aeroacoustics Conference)*, June 2012. doi: 10.2514/6.2012-2094

[5] Metzger, P. T., "Rocket Exhaust Blowing Soil in Near Vacuum Conditions is Faster than Predicted by Continuum Scaling Laws," *Proceedings of Earth and Space 2016: Engineering, Science, Construction, and Operations in Challenging Environments*, April 2016. doi: 10.1061/9780784479971.007